ELSEVIER

Chemical Engineering Journal 139 (2008) 351–362

Chemical Engineering Journal

www.elsevier.com/locate/cej

Quantitative measurement of gas hold-up distribution in a stirred chemical reactor using X-ray cone-beam computed tomography

Stephan Boden *, Martina Bieberle, Uwe Hampel

Forschungszentrum Dresden-Rossendorf e.V., Institute of Safety Research, P.O. Box 510119, 01314 Dresden, Germany

Received 19 March 2007; received in revised form 10 August 2007; accepted 13 August 2007

Abstract

Cone-beam type X-ray computed tomography (CBCT) is a potential method to measure three-dimensional phase distributions in vessels. An example for that is the measurement of gas profiles in stirred chemical reactors. Such data are highly valuable for the assessment and evaluation of chemical processes, for optimisation of the reactor and stirrer design, and for evaluation of computational fluid dynamics codes used to model the fluid flow and heat transfer in reactive systems. However, there are considerable difficulties for accurate quantitative measurements due to beam hardening and radiation scattering effects. In a theoretical and experimental work we have investigated the non-linear effects of both physical phenomena and developed a suitable measurement setup as well as calibration and software correction methods to achieve a highly accurate measurement of void fraction profiles with CBCT.

Keywords: Cone-beam computed tomography; Gas hold-up measurement; Chemical reactor

1. Introduction

There is a long lasting effort to establish precise but practical measurement techniques for the analysis of multi-phase fluid dynamic processes in chemical reactors [1]. The data obtained by such measurement techniques from either industrial or laboratory scale reactors is extremely valuable for the optimisation of reactor vessels, agitation mechanics, and process control, for the optimal shaping and structuring of catalyst supports, for the prediction of safety relevant events and the design of safety related measures, and most recently also for the provision of reference data for CFD simulations.

One particular question that arises for an operating reactor is that of the spatial distribution of the components, respectively, phases that are involved in the reaction. For many types of processes, e.g. gas–liquid mass transfer operations or gas–liquid mixing, it is the gas hold-up distribution within a fixed or fluidised bed, a solid catalyst structure, a pure liquid, or a liquid-particle suspension, that is of interest. The present work relates to this problem and presents a fast and accurate X-ray measurement approach for the gas hold-up distribution in a reactor with a gas-inducing stirrer. The work has in particular been motivated by the objective to compare measured data with results of CFD simulations.

For the problem of the measurement of gas hold-up and its spatial distribution in chemical reactors many techniques have been proposed in the past. The range of methods extends from liquid level measurement, hot wire anemometry [2], suction probes [3,4], electrical probe measurements [5–7], optical holography [8], particle image velocimetry [9], ultrasound techniques [10], X-ray radiography [11–13], electrical impedance tomography [14,15], positron emission tomography [16], and transmission computed tomography using X-rays or gamma radiation. With no doubt methods based on ionising radiation are the most promising since they are non-invasive, they can achieve a high spatial resolution, and they give linear measurements regardless of the structure complexity inside the vessel. Thus, Veera et al. [17] reported on the use of a γ-ray attenuation technique to measure time-averaged radial gas distribution profiles in an aerated stirred tank from sets of chordal attenuation measurements obtained at different horizontal cross-sections. Bukur et al. [18] used this technique in bubble columns. Kumar et al. [19], Kemoun et al. [20], Thatte et al. [21], and Khopkar et al. [22] reported on gamma ray tomography systems used in bubble columns, stirred vessels and fluidised beds. With their devices radial or two-dimensional time-averaged gas hold-up

* Corresponding author. Tel.: +49 351 260 2159; fax: +49 351 260 2007.
E-mail address: S.Boden@fzd.de (S. Boden).

1385-8947/$ – see front matter © 2007 Elsevier B.V. All rights reserved.
doi:10.1016/j.cej.2007.08.014

profiles have been recorded. The use of X-ray CT for gas hold-up measurements has been described by Pike et al. [23] and recently by Hervieu et al. [24] with application to two-phase flow in a pipe, by Kantzas and Kalogerakis [25], who monitored the fluidisation characteristics of a fluidised bed reactor, by Reinicke et al. [26] and Toye et al. [27], who used it in packed catalyst beds, and by Vinegar and Wellington [28], who measured fluid transport in porous media. All the above-mentioned techniques yield time-averaged rather than instantaneous phase distribution images. Time-resolved tomographic imaging may be possible in the future. Thus, recently Misawa et al. [29] introduced a fast X-ray CT setup that is able to produce slice images of two-phase flows with rates of several hundred images per second which gave for the first time the opportunity to study dynamically changing phase distributions.

In recent years, the development of two-dimensional flat panel imagers brought a considerable improvement to digital radiography and rendered the practical application of X-ray cone-beam computed tomography (CBCT) possible. With CBCT a whole volume density distribution can be reconstructed from a set of two-dimensional radiographs obtained from an object at different projection angles. A first report on the application of this technique to gas distribution measurements in an upward pipe flow was given by Tiseanu and Simon [30]. They used a rotating source-detector setup to derive two-dimensional gas fraction distributions at different flow cross-sections with scanning times of several minutes. No beam hardening and scattering correction measures have been implemented.

For the problem of precise gas hold-up measurement in a stirred chemical reactor we found it inevitably necessary to device special correction steps to account for beam hardening and scattered radiation. Our investigations showed that without such corrections the calculated gas fraction values will display errors of several percent. On the opposite the assumed rotationally symmetric phase distribution in an unbaffled reactor enables a rather fast tomography since one radiographic projection is sufficient to compute a complete axial and radial gas hold-up profile. We found that for our particular reactor geometry a one second period of time integration is sufficient to achieve the required signal-to-noise ratio, which means that dynamic processes with time constants of several seconds, such as changing of the stirrer speed, feeding, extraction, and mixing, can be observed in real time. As another side effect also the reconstruction time becomes considerably smaller with this approach since the backprojection type reconstruction algorithm enables a direct reconstruction of a single axial plane.

2. Measurement setup

2.1. Reactor and evaluation phantom

The CBCT measurements were performed on a laboratory scale cylindrical autoclave reactor Ecoclave 150 (Büchi AG, Switzerland) with a hemispherically shaped bottom. The reactor walls are made of 0.008 m thick borosilicate glass with an inner diameter of 0.08 m. As a stirrer we used a gas-inducing impeller with six blades that is mounted on a hollow shaft. During operation the stirrer speed is precisely computer controlled.

To evaluate the accuracy limits of our measurement approach we built a phantom which models the stirrer together with a three-dimensional gas distribution. One practical problem made the design of this phantom a challenge—we wanted to produce at least two different gas fraction distributions (one known gas distribution plus a reactor volume fully occupied by the fluid to gain a reference data set) without making mechanical changes at the reactor during measurements. This is an important issue, since even minute spatial dislocations of reactor vessel or stirrer in between the reference and the gas distribution measurement will inevitable lead to larger errors in the results. Therefore, we devised the phantom that is sketched in Fig. 1. It consists of nine sets of four-fold stacked hollow acrylic tubes with different inner diameters. These sets are vertically placed around the stirrer shaft in three groups of three identical sets that are at equal radii. The tubes are kept in place by two circular acrylic plates at the top and the bottom. At the bottom the tubes are open to the residual reactor volume whereas at the top they are connected to a closed gas reservoir. At the lower end we have placed a three-blade stainless-steel stirrer model between the tubes. Because the phantom is open only at the bottom side and sealed otherwise the gas remains within the tubes and reservoir while the

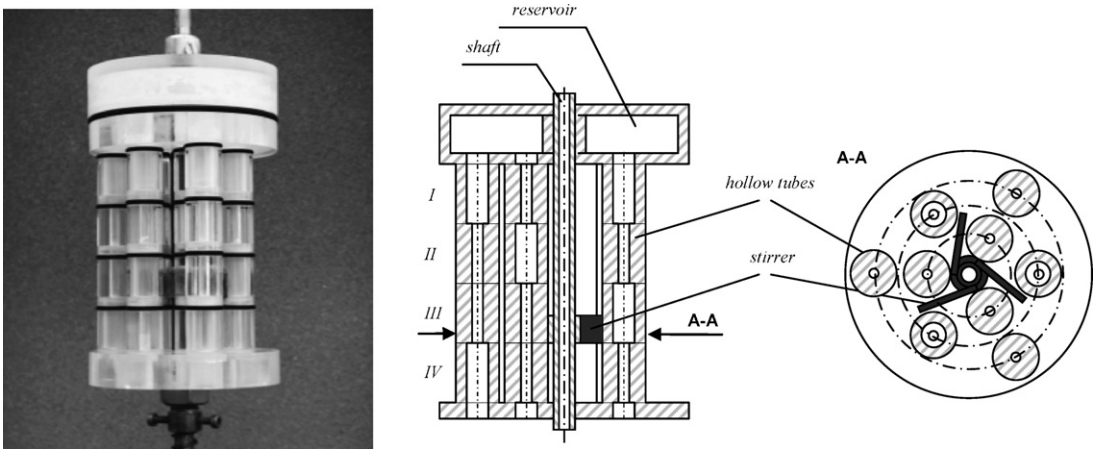

Fig. 1. Performance evaluation phantom.

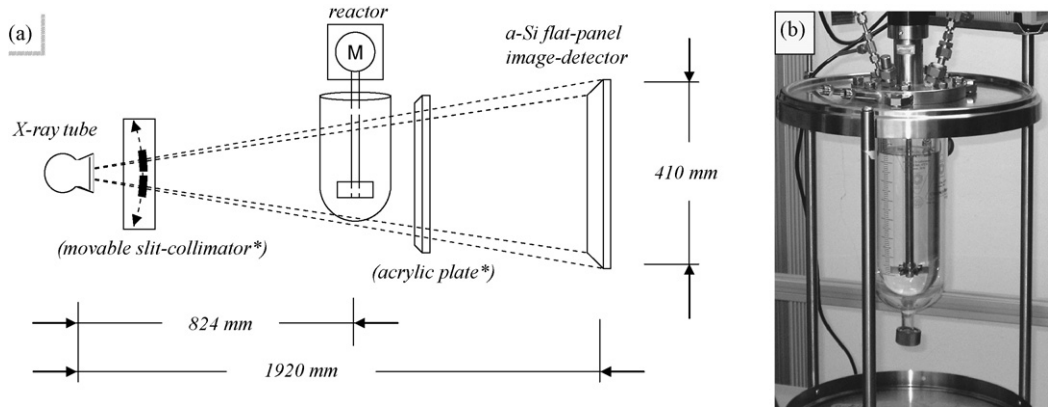

Fig. 2. (a) Schematic CBCT setup. For performance evaluation the stirrer was replaced by the test phantom (*collimator and acrylic plate are required only for calibration). For further explanation see text. (b) Photograph of the stirred tank reactor.

reactor is filled with fluid, which was water during the phantom measurements. By applying a positive operation pressure to the sealed vessel the remaining gas within the phantom becomes compressed and the tubes are filled with fluid. By releasing the operation pressure to normal pressure the remaining gas expands to its initial volume. In this way the gas volume in the tubes of the phantom could be easily adjusted as it was required for the examinations. During measurements the phantom was rotated at an adequate speed, such that the gas-filled tubes appeared as rotationally symmetric gas fraction distributions in the radiograms.

2.2. Measurement setup and data acquisition

The CBCT setup is schematically shown in Fig. 2. As an X-ray source we used a medical type rotating anode X-ray tube DI-104H-22/60-150 (Comet AG, Switzerland) together with an MP601 generator (Röntgenwerk Bochum, Germany) and a two dimensional digital X-ray flat panel detector RID 1640 AL1 (Perkin-Elmer Optoelectronics GmbH & Co. KG, Germany). The X-ray source can be operated at voltages of up to 125 kV and electron currents of maximum 800 mA. The detector has a resolution of 1024 pixels × 1024 pixels, each of 0.4 mm by 0.4 mm size, and can be read out at a maximum rate of 3.5 Hz. The chemical reactor was placed between source and detector at the distances given in Fig. 2a and with its vertical axis coinciding with the vertical centre line of the detector array.

As can be seen in Fig. 3, the flat panel detector displays a delaying behaviour known as image lag. Whereas the applied X-ray pulse is fully rectangular in its intensity, the detector elements have a slower response due to delayed release of trapped electrical charges in each pixel element. The temporal gradient of the release does not depend on the chosen readout rate or frame integration time, respectively (Fig. 3a), nor does it depend on the initial pixel saturation level (Fig. 3b). These findings are contrary to the investigations reported by Siewerdsen and Jaffray [31], who reported different temporal gradients of charge release for varying frame integration times. Our results were observed for our detector by evaluation of the mean pixel-values within a 16 pixel by 16 pixel area close to the centre of the detector for a sequence of 300 frames at different readout rates. For the different readout rates shown in Fig. 3a the X-ray intensities were adjusted so that the mean pixel-value was at about 80% saturation for each readout rate, whereas in Fig. 3b the readout rate was held constant at 0.57 s per frame.

To assure, that the image lag effect does not corrupt measured data, radiographic data acquisition was performed in the way that is illustrated in Fig. 4. Therefore, at first we initiate the acquisition of an image sequence of 130 frames with 3.5 Hz frame rate. After 20 s the X-ray source is switched on with an exposure time of 6.3 s. This is the maximum admissible pulse

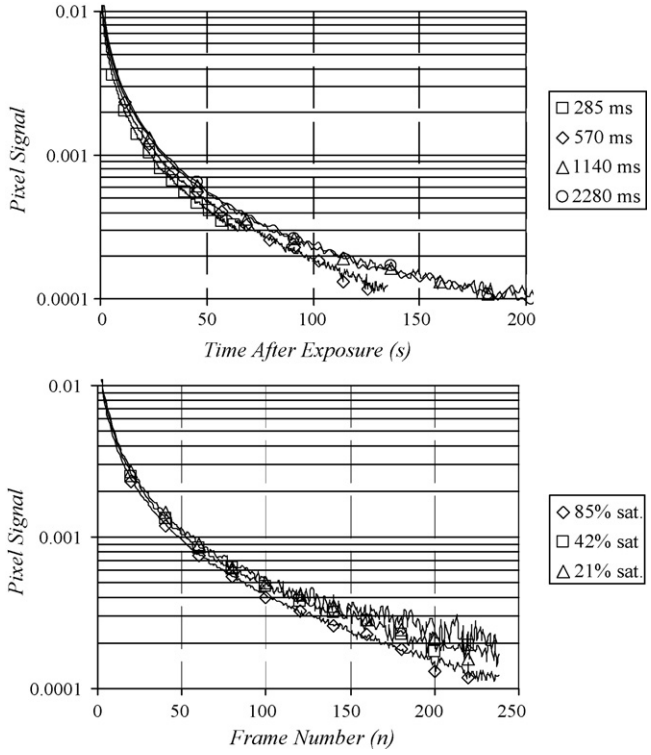

Fig. 3. Dependence of image lag upon readout rate and frame integration time, respectively, and upon pixel saturation. (a) Pixel signal after exposure as a function of time. (b) Pixel signal after exposure as a function of the number of readout cycles for three different initial pixel saturation levels and at a frame integration time of 570 ms.

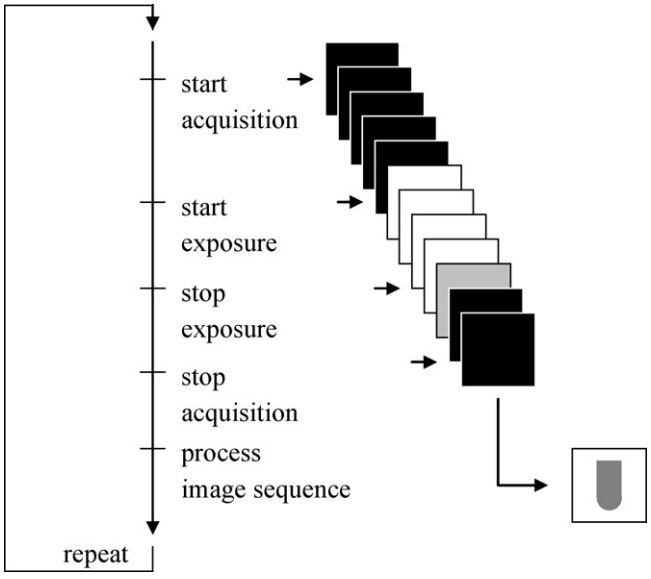

Fig. 4. Operational sequence for the acquisition of a single radiogram.

length of our X-ray generator and gives a sufficiently averaged signal from the rotating liquid–gas mixture in the reactor. The image sequence is then processed in the following way: from averaging of the detector signal between 6 and 20 s we yield the dark current signal. The dark current signal is then subtracted from the subsequently acquired frames. Then, the integral sum of the corrected frames in the time range between 20 and 37 s gives the overall intensity signal for one X-ray pulse and is stored as a single image frame in the computer. After that the resulting image is cropped down to a 460 pixel by 510 pixel region of interest that only covers the phantom inside the reactor.

To reconstruct a gas fraction distribution from the X-ray projection data we applied a differential measurement approach. First of all we acquire a reference intensity image $I^{\varepsilon=0}(\mathbf{r}_S, \mathbf{r}_D)$ of the reactor with gas-free liquid. Then for any acquired intensity image $I^{\varepsilon}(\mathbf{r}_S, \mathbf{r}_D)$ with gas dispersed in the liquid the relationship

$$\begin{aligned}\mathrm{Ext}(\mathbf{r}_S, \mathbf{r}_D) &= -\ln\frac{I^{\varepsilon}(\mathbf{r}_S, \mathbf{r}_D)}{I^{\varepsilon=0}(\mathbf{r}_S, \mathbf{r}_D)} \\ &= -\bar{\mu}^{\mathrm{fluid}}_{\mathrm{eff,S,D}} \int_0^1 \varepsilon(\mathbf{r}_S + t(\mathbf{r}_D - r_S))\,\mathrm{d}t \qquad (1)\end{aligned}$$

holds. Here, $\varepsilon(\mathbf{r})$ is the gas fraction field, $\bar{\mu}^{\mathrm{fluid}}_{\mathrm{eff,S,D}}$ is the effective linear attenuation coefficient of the fluid along the ray path $(\mathbf{r}_S, \mathbf{r}_D)$, $\mathrm{Ext}(\mathbf{r}_S, \mathbf{r}_D)$ is the differential extinction and $\mathbf{r}_S$, $\mathbf{r}_D$ are the spatial coordinates of the source and a given detector pixel. Note, that due to beam hardening effects the effective attenuation coefficient is considered to be ray dependent.

2.3. Reconstruction technique

The inverse problem consists of computing the gas fraction field $\varepsilon(\mathbf{r})$ from the measurements $\mathrm{Ext}(\mathbf{r}_S, \mathbf{r}_D)$. For cone-beam tomography there are two principle approaches to solve this problem. These are exact analytical algorithms and approximate analytical algorithms. The different algorithms have been summarised by Wang et al. [32]. Along with these, there are iterative algebraic reconstruction techniques, which may gain more practical interest in the future for reasons mentioned in [33]. We chose the approximate algorithm which was first suggested by Feldkamp et al. [34]. In the following this algorithm will be referred to as the FDK algorithm.

The FDK algorithm generalises the 2D fan beam tomographic reconstruction with circular source trajectory to the 3D cone-beam tomography. Although widely used, the FDK-algorithm is not exact. There are two reasons for systematic errors in the reconstructed images, these are (a) the violation of the sufficiency condition and (b) the approximations made by Feldkamp et al. The sufficiency condition for 3D cone-beam tomography for an arbitrary source trajectory curve is fulfilled "if and only if every plane which does intersect the object support does intersect the curve at least at one point" (Grangeat [35]). This is not fulfilled for a circular source trajectory as used in our setup. Analytical evaluation of errors caused by violation of this condition is not easy, since the error is due to a partial lack of information in the Radon domain rather than in the Fourier domain. Two major types of artefacts are recognisable in reconstructed images when using the FDK algorithm. At first, surfaces perpendicular to the axis will be blurred to a rhombic shape, and secondly, the reconstructed values are quantitatively to low. Both types of artefacts have an increasing magnitude for planes with increasing distance from the central horizontal plane or increasing cone angle, respectively. In the central horizontal plane the errors are zero. The half-cone angle in our application is less than 3°. This is a rather low value that keeps the mentioned errors quite small in magnitude. For this reason and due to the fact that the FDK algorithm is computationally very efficient we decided to use it to solve our inverse problem.

The FDK algorithm is essentially a modified backprojection algorithm. To recover an object distribution $f(\mathbf{r})$ within the restricted support region, one has to horizontally filter and backproject the measured cone-beam projection data after the proper modification of the voxel-to-source distance and the angular differential. The value of a voxel is then the sum of contributions from all horizontally tilted fan beams passing through the voxel, and can be written as ([36]):

$$f(\mathbf{r}) \approx \frac{1}{2}\int_{\varphi=0}^{\varphi=2\pi}\left[H \times \frac{\|\mathbf{r}_S\|}{\|\mathbf{r}_D - \mathbf{r}_S\|} Xf(\mathbf{r}_S, \mathbf{r}_D)\right]\frac{\|\mathbf{r}_D - \mathbf{r}_S\|^2}{\|\mathbf{r} - \mathbf{r}_S\|^2}\mathrm{d}\varphi, \qquad (2)$$

where $Xf(\mathbf{r}_S, \mathbf{r}_D)$ is the corresponding X-ray transform, H is the horizontal convolution kernel corresponding to the ramp-filtering in frequency domain, and φ is the projection angle. Details of the computation of $Xf(\mathbf{r}_S, \mathbf{r}_D)$ from $\mathrm{Ext}(\mathbf{r}_S, \mathbf{r}_D)$ and the interpretation of $f(\mathbf{r})$ in the context of the gas distribution measurement are given below.

We assume that our examined object – the time-averaged gas distribution field in the stirred chemical reactor – is rotationally symmetric. For simplification, we further require that the axis of symmetry lays perpendicular to the plane of the circular source trajectory. Also, the detector plane has to be perpendicular to the vector $\mathbf{r}_S$. The X-ray transform $Xf(\mathbf{r}_S, \mathbf{r}_D)$ is then no

longer dependent on the projection angle φ of the setup. Thus, from a single measurement $Xf(\mathbf{r}_{S,0}, \mathbf{r}_D)$ and from a set of virtual source positions $\mathbf{r}_{S,virt}$ with $\mathbf{r}_{S,virt}(\varphi=0)=\mathbf{r}_{S,0}$ the rotationally symmetric distribution can be reconstructed as follows:

$$f(\mathbf{r}) \approx \frac{1}{2}\int_{\varphi=0}^{\varphi=2\pi}\left[H \times \frac{\left\|\mathbf{r}_{S,virt}\right\|}{\left\|\mathbf{r}_D - \mathbf{r}_{S,virt}\right\|} Xf(\mathbf{r}_{S,0}, \hat{\mathbf{r}}_D)\right] \times \frac{\left\|\mathbf{r}_D - \mathbf{r}_{S,virt}\right\|^2}{\left\|\mathbf{r} - \mathbf{r}_{S,virt}\right\|^2} d\varphi, \quad (3)$$

where $\hat{\mathbf{r}}_D$ is the translated detector element position of the virtual setup $(\mathbf{r}_{S,virt}, \mathbf{r}_D)$ to the corresponding ray $(\boldsymbol{r}_{S,0}, \hat{\boldsymbol{r}}_D)$.

We implemented the FDK algorithm according to Eq. (3) for the reconstruction of a rotationally symmetric object distribution. In such way we are able to directly compute only radial and axial gas hold-up distributions in the central vertical slice with a considerably reduction in computational load. The algorithm has been implemented in C++ according to the algorithmic description given by Kak and Slaney [37] and takes 66 s CPU time for 512 voxels × 512 voxels to be solved for the rotationally symmetric case. The code utilises full precision floating point arithmetics, and bilinear interpolation is used to sample the filtered two-dimensional projection data at the appropriate positions. These positions according to the ray path geometry are re-calculated for every voxel position at every angular step. Although this prolongs the time to 9.5 h for a full 3D reconstruction of 512 voxels × 512 voxels × 512 voxels from 512 independent projections, this re-calculation efficiently enables us to consider geometrical misalignment of the measurement setup during the reconstruction of the data from full 3D tomographic scans.

2.4. Scattered radiation correction

Scattered radiation emerges as X-rays penetrate the reactor vessel. The contribution of scattered radiation to the detector measurements in CBCT will ultimately lead to quantitative errors in the reconstruction process if not corrected. A known method to cope with scattered radiation is to obtain the intensity profile of scattered radiation and to correct the radiographic image or projection data by that amount. Suggested estimation techniques are Monte-Carlo simulations (Inoue [38]) and deconvolution calculations (Seibert [39]). Another approach is the indirect estimation of scatter by incorporation of an additional radiographic measurement, which should give an almost scatter-free radiograph of the examined object. We have used the latter approach, i.e. a moving slit technique (Jaffe and Webster [40]). Therefore, we placed a horizontal slit collimator in the ray cone just in front of the X-ray tube as shown in Fig. 2a. The 1.5 mm wide slit limits the illumination of the object and detector array to a thin radiation fan. In this way less than four percent of the reactor is exposed to radiation which in turn reduces the scattering offset for about more than 96%. The slit collimator is revolved in small steps of 0.25 mm by means of a computer-controlled stepper motor drive and for each step a radiogram is taken. In this way we scan the whole reactor at full liquid level and moderate stirrer rotation and can thus synthesise a scattering free image of the reactor. The synthetic image is then compared to an image obtained without the slit collimator. The difference of both images gives the scattering offset $I_{sc}^{\varepsilon=0}(\boldsymbol{r}_S, \boldsymbol{r}_D)$ with

$$I_{sc}^{\varepsilon=0}(\mathbf{r}_S, \mathbf{r}_D) = I^{\varepsilon=0}(\mathbf{r}_S, \mathbf{r}_D) - I^{slit,\varepsilon=0}(\mathbf{r}_S, \mathbf{r}_D) \quad (4)$$

which is hereafter subtracted from all subsequent measurements according to

$$I_p(\mathbf{r}_S, \mathbf{r}_D) \approx I(\mathbf{r}_S, \mathbf{r}_D) - I_{sc}^{\varepsilon=0}(\mathbf{r}_S, \mathbf{r}_D) \quad (5)$$

Here, the index sc denotes the scattering offset, and index p denotes the intensity of unscattered radiation along the primary ray path. This approach is reasonable, since by dispersing little amount of gas into the fluid, the overall mass of the object is conserved and there are only slight changes in the material distribution which does not significantly change the scattering offset.

Further, using the same setup, scattering profiles of the actually aerated reactor vessel can be obtained, too. In a supplementary study the variations of the scattering offset due to the aeration were analysed by direct comparison to the profile of the gas-free vessel. It is obvious, that this alternatively obtained scattering profile enables a more accurate correction of intensity measurements for the aerated vessel. Thus, a corresponding reconstruction of the gas distribution was performed in order to evaluate the impact of the only slightly different scattering offsets on the results. The outcome of this study is also given in Section 3.

2.5. Beam hardening correction

Polyenergetic X-ray radiation will be hardened when penetrating thick materials, that is the effective attenuation coefficient becomes smaller with increasing penetration depth. If uncorrected this leads to systematic errors in quantitative X-ray measurements. Our method to perform beam hardening correction addresses the X-ray energy spectra deformation in the measurement of the projection data with respect to the position of each individual ray path. Therefore, we take two radiograms, one of the reactor completely filled with the fluid and another for the same arrangement plus an additional acrylic plate of thickness d^{slab} between reactor vessel and detector as illustrated in Fig. 2. Both images are synthesised from a series of slit images according to the method described above, and thus are assumed to be almost free of scattered radiation. From both images we compute the extinction radiogram

$$Ext_c(\mathbf{r}_S, \mathbf{r}_D) = -\ln\frac{I_p^{\varepsilon=0+slab}(\mathbf{r}_S, \mathbf{r}_D)}{I_p^{\varepsilon=0}(\mathbf{r}_S, \mathbf{r}_D)} = \mu_{eff,S,D}^{slab}\frac{d^{slab}}{\cos\beta_{S,D}} \quad (6)$$

where $\beta_{S,D}$ denotes the angle between the ray and the detector normal, and $\mu_{eff,S,D}^{slab}$ is the observed effective attenuation coefficient of the plate's material. The contribution of such a thin slab to the overall beam hardening is negligible, as is a moderate variation of the gas fraction within the vessel (see Appendix A).

Now the plate is removed, and any image taken from the reactor with another fluid-gas distribution inside is processed to the extinction radiogram

$$\mathrm{Ext}(\mathbf{r}_S, \mathbf{r}_D) = -\ln \frac{I_p^{\varepsilon}(\mathbf{r}_S, \mathbf{r}_D)}{I_p^{\varepsilon=0}(\mathbf{r}_{S,0}, \hat{\mathbf{r}}_D)} \approx -\ln \frac{I^{\varepsilon}(\mathbf{r}_S, \mathbf{r}_D) - I_{sc}^{\varepsilon=0}(\mathbf{r}_S, \mathbf{r}_D)}{I_p^{\varepsilon=0}(\mathbf{r}_{S,0}, \hat{\mathbf{r}}_D)} \quad (7)$$

Taking the ratio of both extinction radiograms gives

$$\frac{\mathrm{Ext}(\mathbf{r}_S, \mathbf{r}_D)}{\mathrm{Ext_c}(\mathbf{r}_S, \mathbf{r}_D)} = \frac{-\bar{\mu}_{\mathrm{eff,S,D}}^{\mathrm{fluid}} \int_0^1 \varepsilon(\mathbf{r}_S + t(\mathbf{r}_D - \mathbf{r}_S))\,\mathrm{d}t}{\mu_{\mathrm{eff,S,D}}^{\mathrm{slab}} d/\cos\beta_{S,D}} \approx -\frac{\bar{\mu}_{\mathrm{eff}}^{\mathrm{fluid}}}{\mu_{\mathrm{eff}}^{\mathrm{slab}}} \frac{\cos\beta_{S,D}}{d} \int_0^1 \varepsilon(\mathbf{r}_S + t(\mathbf{r}_D - \mathbf{r}_S))\,\mathrm{d}t \quad (8)$$

Note that in Eqs. (1) and (6), both $\bar{\mu}_{\mathrm{eff,S,D}}^{\mathrm{fluid}}$ and $\mu_{\mathrm{eff,S,D}}^{\mathrm{slab}}$ are considered to be ray dependent due to beam hardening, whereas on the right hand side of Eq. (8) the ratio $\bar{\mu}_{\mathrm{eff}}^{\mathrm{fluid}}/\mu_{\mathrm{eff}}^{\mathrm{slab}}$ is considered to be ray and thus energy independent. This is reasonably accurate for materials with similar radiological properties, such as PMMA and organic fluids or water (see Appendix A).

To recover the gas fraction distribution from the measurements, Eq. (8) has to be adapted in the following way:

$$Xf(\mathbf{r}_S, \mathbf{r}_D) = -\frac{E(\mathbf{r}_S, \mathbf{r}_D)}{E_c(\mathbf{r}_S, \mathbf{r}_D)} \frac{\mu_{\mathrm{eff}}^{\mathrm{slab}}}{\bar{\mu}_{\mathrm{eff}}^{\mathrm{fluid}}} \frac{d}{\cos\beta_{S,D}} = \int_0^1 \varepsilon(\mathbf{r}_S + t(\mathbf{r}_D - \mathbf{r}_S))\,\mathrm{d}t. \quad (9)$$

Then the X-ray transform $Xf(\mathbf{r}_S, \mathbf{r}_D)$ according to Eq. (9) is then inserted into Eq. (3). This gives the resultant field distribu-

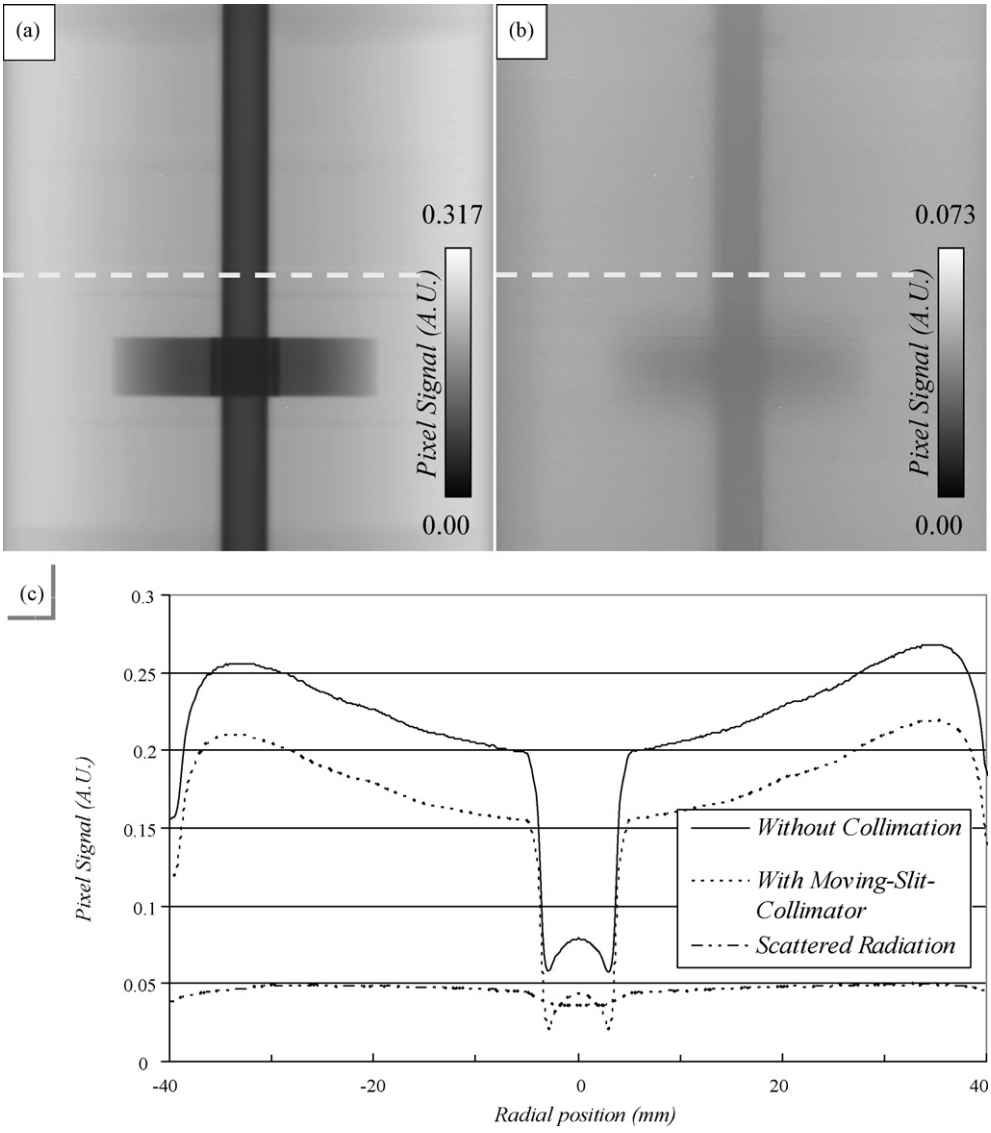

Fig. 5. Measurement of scattered radiation offset. (a) Pixel signal of the fluid-filled rotating phantom inside the vessel (no collimation, 1.0 A.U. = saturated pixel signal). (b) Scattering offset computed from (a) and an additional moving slit measurement. (c) Pixel signal along dashed-line in (a) and (b). The difference between the uncollimated (solid line) and the moving slit (dashed line) signal gives the scattering offset (dash-dotted line).

tion $f(\mathbf{r})$ which is the gas fraction distribution $\varepsilon(\mathbf{r}) = f(\mathbf{r})$ in the vessel.

2.6. Considerations on uncertainty due to noise

Limitations of the quantitative resolution in our measurement approach result from statistical errors due to noise and systematic errors due to approximations inherent in our algorithm. Here the statistical limitations will be described. A quantitative analysis of both types of errors will be presented in the last section.

For analysis, each measured intensity value $I(\mathbf{r}_S, \mathbf{r}_D)$ is treated as an independent random variable. The presented approach mainly utilises the three measured quantities I_p^{ε}, $I_p^{\varepsilon=0}$ and $I_p^{\varepsilon=0+\text{slab}}$. For convenience, ray path coordinates are omitted in the following. Since the reference measurements $I_p^{\varepsilon=0}$ and $I_p^{\varepsilon=0+\text{slab}}$ may be performed with rather longer integration times we may consider the variance of those quantities as being very small and thus negligible. Thus, the variance of the extinction ratio according to Eq. (8) for each pixel element

$$\sigma^2\left(\frac{\text{Ext}}{\text{Ext}_c}\right) = \left|\frac{\partial(\text{Ext}/\text{Ext}_c)}{\partial I_p^{\varepsilon}}\right|^2 \sigma^2(I_p) + \left|\frac{\partial(\text{Ext}/\text{Ext}_c)}{\partial I_p^{\varepsilon=0}}\right|^2 \sigma^2(I_p^{\varepsilon=0}) + \left|\frac{\partial(\text{Ext}/\text{Ext}_c)}{\partial I_p^{\varepsilon=0+\text{slab}}}\right|^2 \sigma^2(I_p^{\varepsilon=0+\text{slab}}),$$

becomes approximately

$$\sigma^2\left(\frac{\text{Ext}}{\text{Ext}_c}\right) \approx \frac{1}{\text{Ext}_c^2 I_p^{\varepsilon}} = \frac{1}{\text{Ext}_c^2}\sigma^2(\text{Ext}). \tag{10}$$

Since Ext_c^2 is much lower than 1.0 in our configuration, the noise level in such calibrated projections Ext/Ext_c will be greater than in uncalibrated measurements of Ext. Ext_c depends on the thickness of the calibration plate. Making this thicker will reduce noise but will also introduce additional amount of beam hardening. Thus, the plate thickness has to be chosen with care.

Using only one time-averaged projection frame of the rotationally symmetric gas distribution instead of using multiple independent projection frames of the same gas distribution can be understood as rotationally averaging the reconstruction result. Noise and thus error propagation from one intensity measurement into the tomographic result via the reconstruction algorithm is thus not an almost space invariant function as in tomography using different angular measurements [41]. Because of the greater circumference, rotationally averaging results in much better noise characteristics for voxels residing at the outer boundary of the circular reconstruction grid. Presuming a discrete radial distance variable i, the standard deviation of the rotationally averaged reconstructed gas fraction value improves as follows:

$$\sigma(\varepsilon') \approx \frac{1}{\sqrt{\pi(2i+1)}}\sigma(\varepsilon), \qquad i = 0, 1, 2, \ldots, n, \tag{11}$$

where it is assumed, that the corresponding horizontal projection was sampled at at least $\pi(2n+1)$ positions. Here $\sigma(\varepsilon')$ denotes the standard deviation of rotationally averaged voxel values, and $\sigma(\varepsilon)$ the standard deviation of reconstructed voxels from independent projection frames. Precision can be further increased by integrating the gas fraction value over larger radial and axial areas or alternatively by increasing X-ray power.

3. Results and discussion

At first, the additional intensity offset of scattered radiation to the detector measurements was determined by the moving slit technique according to Section 2.3. Fig. 5a depicts the radiographic image of the phantom inside the reactor. Fig. 5b shows the computed scattered radiation offset extracted from measurements according Eq. (4). Fig. 5c eventually shows the pixel signal along the dashed line in Figs. 5a and b. The scattered radiation offset is almost equally distributed and its magnitude is about 30% of the uncollimated cone-beam intensity measurements. The drop of scattered radiation behind the shaft and stirrer blades is explained as the result of the high absorption coefficient of the steel which affects even the scattered photons. Such a sharp projection of the inner metallic parts leads to the conclusion, that the scattered radiation emerging from the vessel consisting of a borosilicate glass wall is mainly emitted in a forward directed narrow cone.

The plate for the beam hardening correction and calibration according to Section 2.5 was made of PMMA (polymethylmetaacrylate) and was 0.01 m in thickness. Fig. 6 shows the measured attenuation coefficients, mapped for each source to pixel X-ray pencil beam $(\mathbf{r}_S, \mathbf{r}_D)$ according to Eq. (6). Although the plate is of constant thickness and material, and scattered

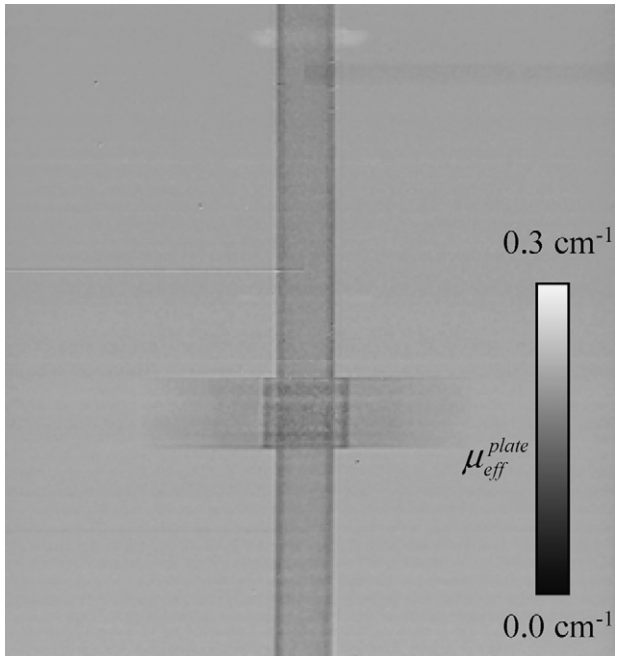

Fig. 6. Measured attenuation coefficient map of a 1 cm thick acrylic plate. The tube voltage was 125 kV.

radiation is removed by application of the moving slit technique to both intensity measurements, the positions of the metallic structures are clearly recognisable in the projection image, as at these positions the attenuation coefficient map of the acrylic plate shows decreased values. This can easily be understood, since the metallic parts cause a much stronger beam hardening then the remaining vessel. The measured image as shown in Fig. 6 is then used for subsequent beam hardening correction and calibration according to Eq. (8).

Eventually, gas was filled into the phantom holes and the gas distribution measurement was carried out. After data acquisition and preprocessing, the time-averaged single projection frame was fed into the FDK CBCT solver. For calculations of absolute gas fractions the ratio $\mu_{\text{eff}}^{\text{slab}}/\bar{\mu}_{\text{eff}}^{\text{fluid}}$ was set to be $\mu_{\text{eff}}^{\text{slab}}/\bar{\mu}_{\text{eff}}^{\text{fluid}} = 1.13$ for water and $\mu_{\text{eff}}^{\text{slab}}/\bar{\mu}_{\text{eff}}^{\text{fluid}} = 1.45$ for isopropanol as fluid [42]. These values hold for an effective mean X-ray energy of 80 keV, and only slightly vary (less than 1.1% for water, less then 0.2% for isopropanol) within a range of photon energies expected at our setup. The reconstruction of one half of the central vertical slice (230 voxels by 510 voxels) took 47 s for 800 virtual source positions on a 2 GHz AMD Athlon processor desktop computer.

Fig. 7a shows the differential extinction radiogram and Fig. 7b the measured time-averaged gas distribution of the rotating phantom. The four layers defined by the different phantom tube configurations are clearly recognisable. This figure is a grey-scale representation of the gas fraction values of the vertical central slice composed of voxels of size $(200\,\mu\text{m})^3$. Since we assume radial symmetry, we expect no gas fraction variation in the vertical direction within each layer. So, for further analysis, we manually selected rectangular regions with a height of 30 rows within each layer, whereby layer III was further subdivided into the region inside and the region outside the outer impeller radius. In these regions we compared the numerically calculated

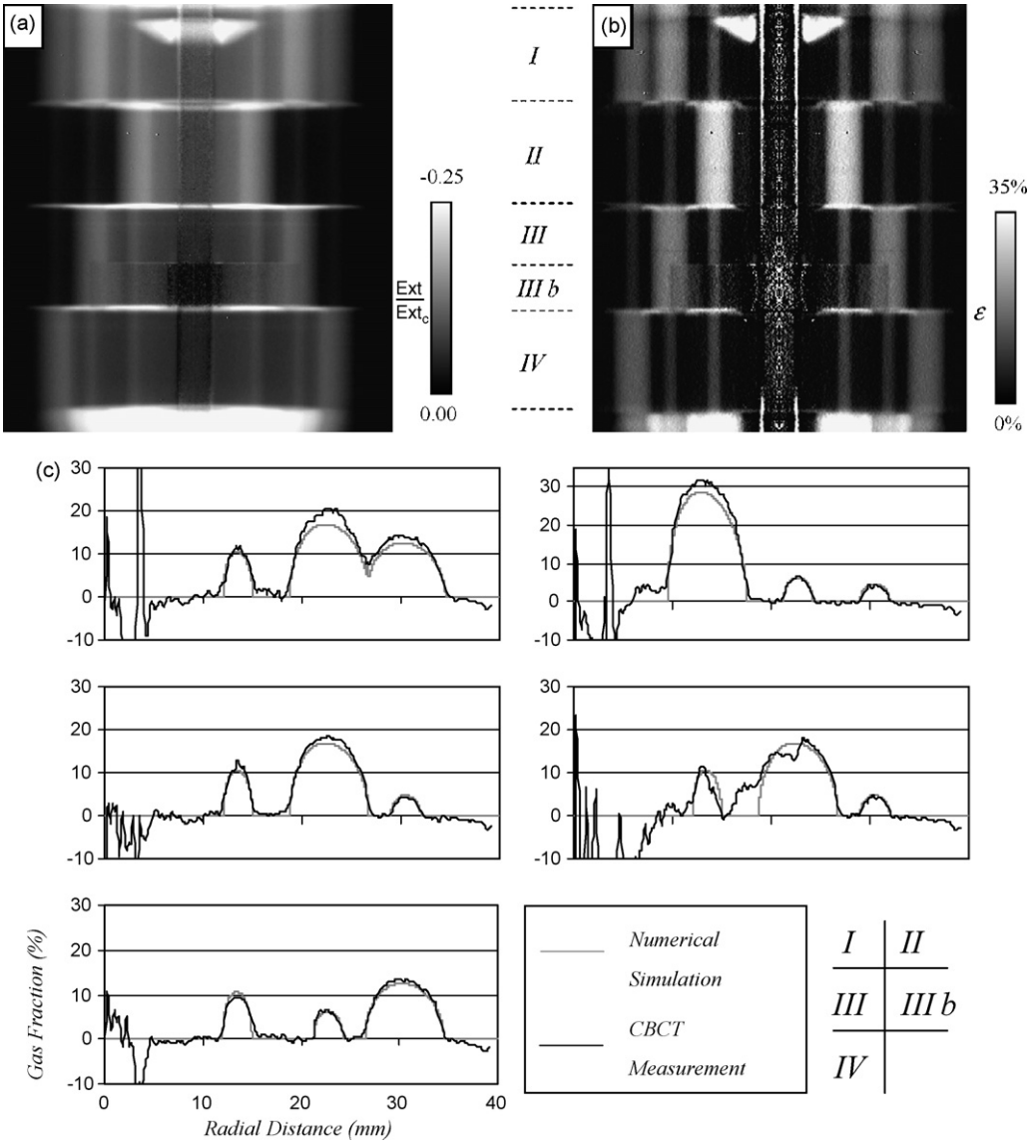

Fig. 7. (a) Calibrated extinction map of the fluid filled phantom. (b) Reconstructed central vertical slice. The grey-scale corresponds to the void fraction distribution in the phantom. (c) Radial gas fraction distribution of the phantom in five different regions according to (b). Therefore, the measured data was averaged over 30 rows.

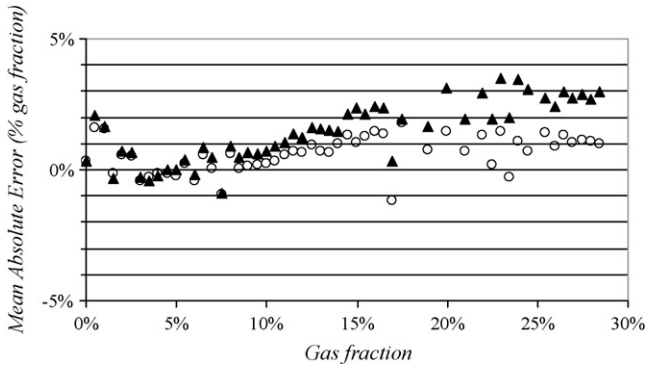

Fig. 8. Systematic mean absolute error of the phantom's reconstructed gas distribution (Fig. 7b). Black triangles denote the error according to the proposed method; open circles denote an improved performance using the moving slit method not only for the reference measurements (see text).

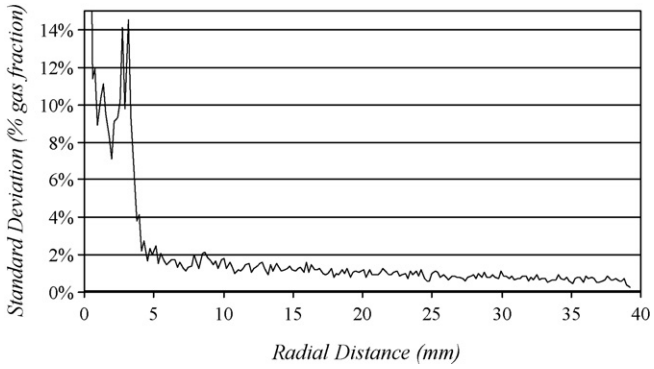

Fig. 9. Standard deviation of the reconstructed gas distribution (Fig. 7b) due to statistical fluctuations as a function of radial distance.

gas fraction values to the measured gas fraction of the phantom averaged over the 30 rows. The result is shown in Fig. 7c. The measured values show a very good agreement with the expected values in terms of gas fraction magnitude as well as in terms of spatial resolution. Only layer III b that represents the region in between the stirrer blades shows some deviations, which are due to still insufficient correction for scattered radiation.

For all of the five regions, the voxels from Fig. 7b are then classified by their simulated gas fraction value. As specified by the phantom, only gas fractions below 30% are considered. For each class, the mean of the absolute measurement error which is the difference between measured and simulated gas fraction is computed and presented in Fig. 8 (black triangles). The systematic error remains below 3.5% in absolute gas fraction and becomes much better for smaller gas fraction values. This residual error is obviously due to still imperfect correction schemes for beam hardening and scattered radiation. However, using the present measurement approach, we are not able to differentiate the contributions to the remaining error, which is noteworthy quite low, since none of the causes can be completely separated from the others.

Along with these systematic errors, which were evaluated as an average mean error over a class of voxels, there are statistical uncertainties in the reconstruction which are due to the presence of noise in the radiographic data. Unfortunately, due to the radial averaging property of the reconstruction technique the resulting statistical uncertainties are non-uniformly distributed along the reconstructed slice images. This prevents us from calculating of uncertainties for the observed local gas fractions directly from the measurement. However, for evaluation, the standard deviation of the voxel values along the columns, i.e. the different radii, was calculated and is displayed in Fig. 9. The statistical uncertainty shows the spatial dependence that was expected according to Eq. (11). It drops rapidly below 2% in absolute gas fraction and even below 1% in absolute gas fraction the more distant the radial positions becomes. Due to the low signal-to-noise ratio in the region behind the stirrer shaft there is a strong uncertainty in that region, which makes an accurate determination of absolute gas fraction values within the hollow stirrer shaft impossible.

In a supplementary study, also the scattering radiation profile for the gas-filled phantom was measured. Only slight variations in the scattering intensity in comparison to previously measured were observed. These variations are less than 4% in magnitude for local gas fraction differences of maximum 30%. Further, this additionally obtained scattering profile was used to correct the intensity measurements of the aerated phantom. The resulting errors of a corresponding gas distribution reconstruction are included in the plot of Fig. 8 as open circles. As expected, the systematic error was further decreased, down to 1.5% at maximum, but the overall measurement time increased to 25 min. However, although the maximum measurement error without this additionally obtained scattering profile was less than 3.5% (for local gas fractions up to 30%) and thus was notable small, the authors suggest the application of the moving slit technique to all involved radiographic intensity measurements, if higher gas fractions along the ray paths are expected.

The phantom measurements have been performed to evaluate the accuracy of our CBCT technique with respect to gas fraction measurement in the reactor. After that we performed a series of measurements on the laboratory reactor at real stirring operation. The model fluid we used was isopropanol at normal pressure and room temperature. The critical stirrer speed when gas dispersion at the stirrer blades starts has been estimated by optical observation to be at 1020 rpm. Then the stirrer was successively driven with speeds in the range of 1000–1200 rpm at 50 rpm intervals. For each operation point we performed a CBCT scan as described above. The resulting gas fraction profiles are shown in Fig. 10. Beside the fact, that the precise high-resolution gas fraction profiles are valuable data for CFD code evaluation we also found a few further interesting characteristics in the images. First, it should be noted that the CBCT technique does well resolve the central vortex about the stirrer shaft where the gas fraction values are close to 100%. The transition region between the gas fraction values of 100 and 0% at the surface of the vortex contains information on the amplitude of surface waves that are observable at the gas–liquid interface. Further, it should be noted that the gas tends to concentrate about the stirrer shaft, its tip and within the radial region between the stirrer blades and the reactor wall, where it is confined by the turbulent flow field.

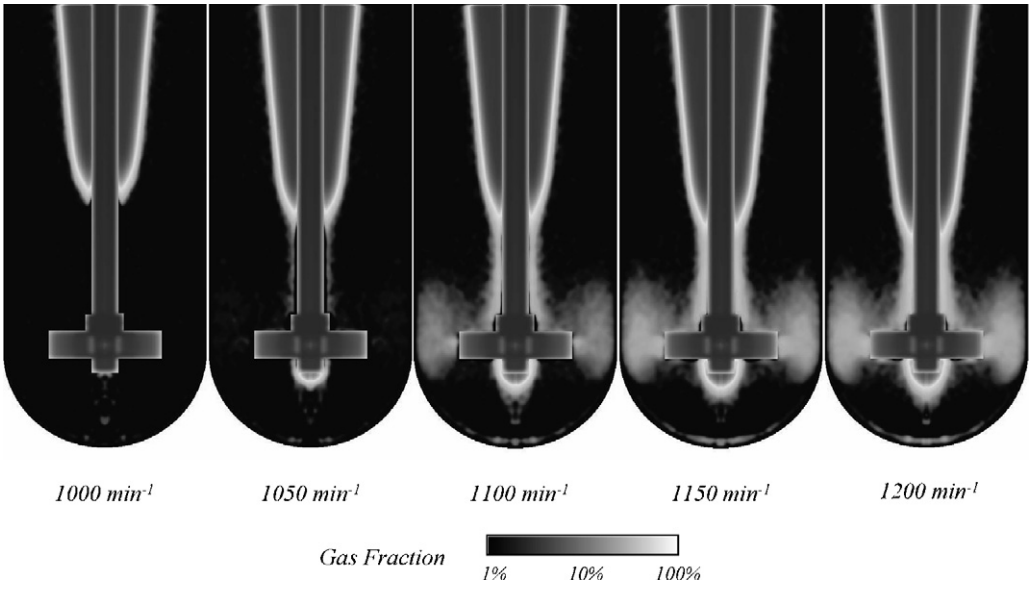

Fig. 10. Measured gas fraction distributions in the stirred reactor at different stirrer speed (logarithmic grey-scale).

4. Conclusion

We presented a fast three-dimensional tomographic measurement technique for the measurement of gas distributions in stirred vessels. The high accuracy in time-average phase fraction distribution is achieved by proper and practical correction measures for the problems of beam hardening and radiation scattering. By measurements on a special evaluation phantom we could show that the accuracy in gas fraction values is better then 3.5% for a single voxel of size 200 μm. Thus, this method gives a superior spatial resolution at short scanning times. The rotating fluid-gas distribution inside a stirred reactor offers the opportunity to considerably reduce scanning time and computational reconstruction effort by assuming rotational invariance of the distribution and consequently computing only the gas fraction distribution for a central vertical slice. It should be pointed out here, that the method can be straightforward extended to the measurement of non-symmetrical phase fraction distributions just by proper rotation of either the X-ray setup or the vessel. In such a case, as for example with baffled stirred vessels or column reactors, the scanning time and the computational burden for a full 3D image reconstruction would increase correspondingly, however, spatial resolution and gas fraction accuracy will be of the same order as for the case of radial symmetry. For the future we expect that this method will be used to provide valuable reference data for CFD calculations and CFD model improvements that are done concurrently.

Appendix A. Sensitivity of the effective attenuation coefficients

In Section 2.5, for beam hardening correction we devised a reference absorber method. Here, we will address the problem whether the gas content, which is the only variable parameter between a reference and a real measurement, has any influence on the beam hardening correction algorithm and must be taken into account. Therefore, we performed the following theoretical study. At first consider the detected intensities of two pencil like X-ray beams, ray#1 and ray#2, one penetrating the fluid filled vessel and its walls (ray#1) and one additionally penetrating the hollow stirrer shaft (total 2 mm steel) (ray#2), for varying total gas fractions along a chord path S,D,

$$\varepsilon_{\mathrm{S,D}} = \frac{1}{d^{\mathrm{fluid}}_{\mathrm{S,D}}} \int_0^1 \varepsilon(\mathbf{r}_{\mathrm{S}} + t(\mathbf{r}_{\mathrm{D}} - \mathbf{r}_{\mathrm{S}}))\,\mathrm{d}t. \tag{12}$$

The intensities of the emerging beams are calculated by integration over the energies E according to

$$I^{\varepsilon}(\mathbf{r}_{\mathrm{S}}, \mathbf{r}_{\mathrm{D}}) = \int W(E) I_{\mathrm{S}}(E) \exp\left\{ -\sum \mu^{\mathrm{m}}(E) d^{\mathrm{m}}_{\mathrm{S,D}} - \mu^{\mathrm{fluid}}(E) d^{\mathrm{fluid}}_{\mathrm{S,D}} (1 - \varepsilon_{\mathrm{S,D}}) \right\} \mathrm{d}E. \tag{13}$$

For the initial spectral intensity distribution $I_{\mathrm{S}}(E)$ of the source the energy spectrum of a tungsten X-ray tube [43] with an additional 2.45 mm Al pre-filtering was used. For the detector's conversation efficiency, $W(E)$, a simplified model was used which is given by the probability of the attenuation of an X-ray photon in the detectors scintillator material and by the

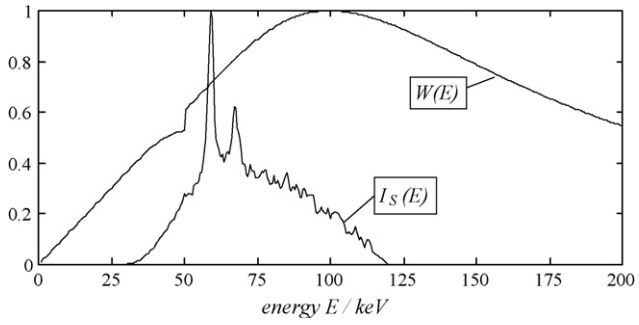

Fig. 11. Normalised spectral distribution curves of the X-ray source $I_{\mathrm{s}}(E)$ [43] and detector's conversion efficiency $W(E)$ models.

Table 1
Evaluation of the effective linear attenuation coefficients for isopropanol (water) and for the calibration slab made from acryl glass for two different ray paths (see text) based on a model of our experimental setup

	Ray#1	Ray#2	
$\bar{\mu}^{\text{fluid}}_{\text{eff,S,D}}$	0.1484 (0.1906)	0.1423 (0.1816)	4.3% (4.9%)
$\max\left(\frac{\mu^{\text{fluid}}_{\text{eff,S,D}}(\varepsilon_{\text{S,D}})-\bar{\mu}^{\text{fluid}}_{\text{eff,S,D}}}{\bar{\mu}^{\text{fluid}}_{\text{eff,S.D}}}\right)\Big\vert_{0<\varepsilon_{\text{S,D}}\leq 0.5}$	0.38% (0.74%)	0.19% (0.35%)	
$\mu^{\text{slab}}_{\text{eff,S,D}}$	0.2152 (0.2130)	0.2060 (0.2051)	4.4% (3.8%)
$\frac{\bar{\mu}^{\text{fluid}}_{\text{eff,S,D}}}{\mu^{\text{slab}}_{\text{eff,S,D}}}$	0.6898 (0.8947)	0.6907 (0.8854)	0.2% (1.1%)

The rightmost column displays the difference of the values between ray#1 and ray#2 relative to their mean.

production of a signal which is proportional to the energy of the incident photons. Both $W(E)$ and $I_{\text{S}}(E)$ are depicted in Fig. 11. With $m = \{\text{wall, shaft}\}$, μ^{wall}, μ^{shaft}, and μ^{fluid} denote the total linear attenuation coefficients of the vessel's wall, shaft and fluid; and $d^{\text{wall}}_{\text{S,D}} = 1.6\,\text{cm}$, $d^{\text{shaft}t}_{\text{S,D}} = 0.0\,\text{cm}$ (for ray#1, $d^{\text{shaft}}_{\text{S,D}} = 0.2\,\text{cm}$ for ray#2, respectively) and $d^{\text{fluid}}_{\text{S,D}} = 8.0\,\text{cm}$ denote the lengths of the intersection of the ray path with the corresponding material, respectively. The relative change in the overall effective attenuation due to moderate variation of the gas content in the vessel with respect to the fully filled reactor is then expressed by the observed relative extinction

$$\text{Ext}(\varepsilon_{\text{S,D}}) = -\ln\frac{I^{\varepsilon}(\mathbf{r}_{\text{S}}, \mathbf{r}_{\text{D}})}{I^{\varepsilon=0}(\mathbf{r}_{\text{S}}, \mathbf{r}_{\text{D}})} = -\mu^{\text{fluid}}_{\text{eff,S,D}}(\varepsilon_{\text{S,D}}) \cdot d^{\text{fluid}}_{\text{S,D}} \cdot \varepsilon_{\text{S,D}}, \tag{14}$$

whereas an effective attenuation coefficient of the fluid $\mu^{\text{fluid}}_{\text{eff,S,D}}$ was used to correlate the observation with the given gas fraction. Here, $\mu^{\text{fluid}}_{\text{eff,S,D}}$ depends on the material distribution along the ray path S,D. Using Eq. (14), this effective attenuation coefficient of the fluid was then evaluated for varying gas fractions according to

$$\mu^{\text{fluid}}_{\text{eff,S,D}}(\varepsilon_{\text{S,D}}) = -\frac{1}{d^{\text{fluid}}_{\text{S,D}}}\frac{\text{d}\,\text{Ext}(\varepsilon_{\text{S,D}})}{\text{d}\varepsilon}. \tag{15}$$

As a result, for a fixed ray path the maximum deviation of the observed attenuation coefficient from its mean over a reasonable range of gas fractions,

$$\max\left(\frac{\mu^{\text{fluid}}_{\text{eff,S,D}}(\varepsilon_{\text{S,D}}) - \bar{\mu}^{\text{fluid}}_{\text{eff,S,D}}}{\bar{\mu}^{\text{fluid}}_{\text{eff,S.D}}}\right)\Big|_{0\leq\varepsilon_{\text{S,D}}\leq 0.5}, \tag{16}$$

with

$$\bar{\mu}^{\text{fluid}}_{\text{eff,S,D}} = \left\langle \mu^{\text{fluid}}_{\text{eff,S,D}}(\varepsilon_{\text{S,D}}) \right\rangle\Big|_{0\leq\varepsilon_{\text{S,D}}\leq 0.5}, \tag{17}$$

was found to be less then 0.5%. This is small compared to the variations of $\bar{\mu}^{\text{fluid}}_{\text{eff,S,D}}$ for the two different rays ray#1 and ray#2, which on the other hand exceed the limits of 4.0% (both for water (H_2O) or isopropanol ($C_3H_5O_8$) as fluid) (Table 1). In the following we thus consider the effective attenuation coefficient of the fluid as independent on the actual amount of gas.

However, an elaborate calibration of $\bar{\mu}^{\text{fluid}}_{\text{eff,S,D}}$ is required dependent on its position of each particular ray path. Therefore, it would be beneficial to determine the fluids effective attenuation coefficient for the different detector positions. This can be achieved by insertion of an additional thin slab of fluid between the vessel and the detector. Since the exact dimensions of such a slab are known, the determination of the effective attenuation coefficient of the slab's material from two intensity measurements will be immediately possible according to Eq. (6). Then, if the slab is made of the same fluid as that contained in the vessel, the observed attenuation coefficient $\mu^{\text{slab}}_{\text{eff,S,D}}$ is equal to $\bar{\mu}^{\text{fluid}}_{\text{eff,S,D}}$ of the fluid. However, we found it more convenient to use a solid plate of acrylic glass for the respective calibration measurement. Acrylic glass exhibits radiological properties which are very similar to these of water and organic fluids. Therefore, and as found by an investigation of the slab's effective attenuation coefficient according to the Eqs. (17), (15), (14), (13) with $m = \{\text{wall, shaft, slab}\}$ and (6), the ratio between the effective attenuation coefficients for the fluid and the thin slab, $\bar{\mu}^{\text{fluid}}_{\text{eff,S,D}}/\mu^{\text{slab}}_{\text{eff,S,D}}$ is found to be almost constant (Table 1), and $\bar{\mu}^{\text{fluid}}_{\text{eff}}/\mu^{\text{slab}}_{\text{eff}}$ is thus treated as independent on the ray path position for the considered setup.

References

[1] C. Boyer, A.-M. Duquenne, G. Wild, Measuring techniques in gas–liquid and gas–liquid-solid reactors, Chem. Eng. Sci. 57 (2002) 3185–3215.
[2] W.-M. Lu, S.-J. Ju, Local gas holdup, mean liquid velocity and turbulence in an aerated stirred tank using hot-film anemometry, Chem. Eng. J. 35 (1987) 9–17.
[3] M. Barigou, M. Greaves, A capillary suction probe for bubble-size measurement, Meas. Sci. Tech. 2 (1991) 318–326.
[4] M. Kamiwano, M. Kaminoyama, K. Nishi, D. Shirota, The measurement of bubble diameter distributions and liquid side mass transfer coefficients in a gas–liquid agitated vessel using a real-time, high-speed image processing system, Chem. Eng. Commun. 190 (2003) 1096–1114.
[5] K. Takenaka, K. Takahashi, Local gas holdup and gas recirculation rate in an aerated vessel equipped with a rushton turbine impeller, J. Chem. Eng. Jpn. 29 (1996) 799–804.
[6] A. Bombač, I. Žun, B. Filipič, M. Žumer, Gas-filled cavity structures and local void fraction distribution in aerated stirred vessel, AIChE J. 43 (1997) 2921–2931.
[7] A. Paglianti, S. Pintus, An impedance probe for the measurement of liquid hold-up and mixing time in two/three-phase stirred tank reactors, Exp. Fluids 31 (2001) 417–427.
[8] V. Ilchenko, R. Maurus, T. Sattelmayer, Processing and analysis of holographic images for the bubbles characterisation in an aerated stirred tank, in: Proc. Eurotherm 71, Reims, 2002, pp. 137–144.

[9] M. Laakkonen, M. Honkanen, P. Saarenrinne, J. Aittamaa, Local bubble size distributions, gas–liquid interfacial areas and gas holdups in a stirred vessel with particle image velocimetry, Chem. Eng. J. 109 (2005) 37–47.
[10] J. Wolf, Investigation of bubbly flow by ultrasonic tomography, Part. Part. Syst. Charact. 5 (1998) 170–173.
[11] J.B. Romero, D.W. Smith, Flash X-ray analysis of fluidized beds, AIChE J. 11 (1965) 595–600.
[12] P.N. Rowe, D.J. Everett, Fluidized-bed bubbles viewed by X-rays. 1. Experimental details and interaction of bubbles with solid surfaces, Trans. Inst. Chem. Eng. 50 (1972) 42–48.
[13] J.G. Yates, D.J. Cheesman, P. Lettieri, D. Newton, X-ray analysis of fluidized beds and other multiphase systems, KONA Powder Sci. Technol. Jpn. 20 (2002) 133–143.
[14] R.A. Williams, R. Mann, F.J. Dickin, O.M. Ilyas, P. Ying, R.B. Edwards, A. Rushton, Application of electrical impedence tomography to mixing in stirred vessels, AIChE Symp. Ser. 293 (1993) 8–15.
[15] T. York, Status of electrical tomography in industrial applications, J. Electron. Imaging 10 (2001) 608–619.
[16] S.L. McKee, R.A. Williams, A. Boxman, Development of solid-liquid mixing models using tomographic techniques, Chem. Eng. J. 56 (1995) 101–107.
[17] U.P. Veera, A.W. Patwardhan, J.B. Joshi, Measurement of gas hold-up profiles in stirred tank reactors by gamma ray attenuation technique, Trans. IChemE A 79 (2001) 684–688.
[18] D.B. Bukur, J.G. Daly, S.A. Patel, Application of γ-ray attenuation measurement of gas holdup and flow regime transitions in bubble columns, Ind. Eng. Chem. Res. 35 (1996) 70–80.
[19] S.B. Kumar, D. Moslemian, M.P. Dudukovic, A γ-ray tomographic scanner for imaging voidage distribution in two-phase flow systems, Flow Meas. Instrum. 6 (1995) 61–73.
[20] A. Kemoun, B.C. Ong, P. Gupta, M.H. Al-Dahhan, M.P. Dudukovic, Gas holdup in bubble columns at elevated pressure via computed tomography, Int. J. Multiphase Flow 27 (2001) 929–946.
[21] A.R. Thatte, R.S. Ghadge, A.W. Patwardhan, J.B. Joshi, G. Singh, Local gas holdup measurement in sparged and aerated tanks by γ-ray attenuation technique, Ind. Eng. Chem. Res. 43 (2004) 5389–5399.
[22] A.R. Khopkar, A.R. Rammohan, V.V. Ranade, M.P. Dudukovic, Gas–liquid flow generated by a Rushton turbine in stirred vessel: CARPT/CT measurements and CFD simulations, Chem. Eng. Sci. 60 (2005) 2215–2229.
[23] R.W. Pike, B. Wilkins, H.C. Ward, Measurement of the void fraction in two-phase flow by X-ray attenuation, AIChE J. 11 (1965) 794–799.
[24] E. Hervieu, E. Jouet, L. Desbat, Development and validation of an x-ray tomograph for two-phase flow, Ann. N.Y. Acad. Sci. 972 (2002) 87–94.
[25] A. Kantzas, N. Kalogerakis, Monitoring the fluidization characteristics of polyolefin resins using X-ray computer assisted tomography scanning, Chem. Eng. Sci. 51 (1996) 1979–1990.
[26] N. Reinicke, G. Petritsch, D. Schmitz, D. Mewes, Tomographic measurement techniques—visualization of multiphase flows, Chem. Eng. Technol. 21 (1998) 7–18.
[27] D. Toye, P. Marchot, M. Crine, A.-M. Pelsser, G.L. L'Homme, Local measurement of void fraction and liquid holdup in packed columns using X-ray computed tomography, Chem. Eng. Proc. 37 (1998) 511–520.
[28] H.J. Vinegar, S.L. Wellington, Tomographic imaging of three-phase flow experiments, Rev. Sci. Instrum. 58 (1987) 96–107.
[29] M. Misawa, N. Ichikawa, M. Akai, K. Hori, K. Tamura, G. Matsui, Ultra fast X-ray CT systems for measurement of dynamic events in two-phase flow, in: Proceedings of ASME/JSME/SFEN ICONE-6, San Diego, 1998, pp. 508–522.
[30] I. Tiseanu, M. Simon, High-resolution cone-beam tomography for two-phase flow diagnostics, in: Proceedings of the Second International Symposium on Two-Phase Flow Modelling and Experimentation, Pisa, 1999, pp. 1485–1492.
[31] J.H. Siewerdsen, D.A. Jaffray, A ghost story: spatio-temporal response characteristics of an indirect-detection flat-panel imager, Med. Phys. 26 (1999) 1624–1641.
[32] G. Wang, S.Y. Zhao, P.C. Cheng, Exact and approximate cone-beam X-ray microtomography, in: P.C. Cheng, et al. (Eds.), Focus on Multidimensional Microscopy, vol. 1, World Scientific, 1999, pp. 233–261.
[33] T. Nielsen, R. Manzke, R. Proksa, M. Grass, Cardiac cone-beam CT volume reconstruction using ART, Med. Phys. 32 (2005) 851–860.
[34] L.A. Feldkamp, L.C. Davis, J.W. Kress, Practical cone-beam algorithm, J. Opt. Soc. Am. A 1 (1984) 612–691.
[35] P. Grangeat, Mathematical framework of cone beam 3D reconstruction via the first derivative of the Radon transform, Lecture Notes Math. 1497 (1991) 66–97.
[36] P. Rizo, P. Grangeat, P. Sire, P. Lemasson, P. Melennec, Comparison of two three-dimensional X-ray cone-beam-reconstruction algorithms with circular source trajectories, J. Opt. Soc. Am. A 8 (1991) 1639–1648.
[37] A.C. Kak, M. Slaney, Principles of Computerized Tomographic Imaging, IEEE Press, New York, 1988.
[38] K. Inoue, T. Sudou, N. Nakamori, H. Kanamori, M. Endo, Software correction for scattered X-rays on cone-beam CT images, J. Imaging Sci. Tech. 39 (1995) 319–323.
[39] J.A. Seibert, J.M. Noone, X-ray scatter removal by deconvolution, Med. Phys. 15 (1988) 567–575.
[40] C. Jaffe, E.W. Webster, Radiographic contrast improvement by means of slit radiography, Radiology 116 (1975) 631–635.
[41] R.A. Brooks, G. Di Chiro, Statistical limitations in X-ray reconstructive tomography, Med. Phys. 3 (1976) 237–240.
[42] J.H. Hubbel, S.M. Seltzer, Tables of X-ray mass attenuation coefficients and mass-energy-absorption coefficients, online at http://www.physics.nist.gov/PhysRefData/XrayMassCoef.
[43] P. Hammersberg, M. Stenström, H. Hedtjärn, M. Mångård, Absolute energy spectra for an industrial micro focal X-ray source under working conditions measured with a Compton scattering spectrometer – full spectra data, Linköping Electron. Articles Mech. Eng. 1 (1998) 1–13.